Interface engineering of a hollow core-shell sulfur-doped Co₂P@Ni₂P heterojunction for efficient charge storage of hybrid supercapacitors

Xiaoqiu Yue[1], Yingxia Dong[1], Juan Gong[1], Yongbo Gao[1], Kwok Ho Lam[2*], Qiaoji Zheng[1], Dunmin Lin[1*]

[1]*College of Chemistry and Materials Science, Sichuan Normal University, Chengdu 610066, P. R. China*

[2]*Centre for Medical and Industrial Ultrasonics, James Watt School of Engineering, University of Glasgow, Glasgow, Scotland, United Kingdom*

Abstract

Transition metal phosphides (TMPs) are widely used as supercapacitor energy storage materials due to their abundant valence and high theoretical capacity, but their poor electrical conductivity and low active material utilization lead to low actual capacity and slow kinetics. Herein, we demonstrate the excellent electrochemical properties of sulfur-doped Co₂P@Ni₂P heterojunction materials prepared using a combination of hydrothermal, ion-exchange and low-temperature annealing approaches. For sulfur-doped Co₂P@Ni₂P, hollow core-shell microstructures increase the number of electroactive sites and provides a shortcut for electron transport, while sulfur doping

* Corresponding authors: kwokho.lam@glasgow.ac.uk (Kwok Ho Lam); ddmd222@sicnu.edu.cn (Dunmin Lin); Fax: +86 28 84760802; Tel: +86 28 84760802

promotes the transfer and rearrangement of interfacial charge from Co_2P to Ni_2P, optimizing the redox ability of the active component. In addition, the S doping and the highly electrochemically active nickel-cobalt phosphide synergistically accelerate the charge transfer, which leads to fast reaction kinetics. Therefore, the obtained S-$Co_2P@Ni_2P$ exhibits an optimal specific capacity of 1200 C g^{-1} at 1 A g^{-1} and excellent rate performance. Furthermore, when combined with activated carbon (AC) for hybrid supercapacitor (HSC), the S-$Co_2P//AC$ device shows an excellent energy density of 41.5 Wh kg^{-1} and a high-capacity retention of 93% after 15,000 cycles. This work provides a novel approach for the exploration of high-performance and stable phosphorus-based battery-like supercapacitor materials.

Keywords: Sulfur-doping, Hollow core-shell heterojunction, Bimetallic phosphides, Hybrid supercapacitors

1. Introduction

To resolve the problems of fossil fuel consumption and environment, one of the keys is to develop breakthrough efficiency energy storage facilities such as fuel cells and supercapacitors[1-3]. Supercapacitors, as devices dedicated to energy storage, meet the requirements for clean and safe energy storage with high power delivery, extremely long cycle life, and rapid energy collection[4, 5]. The energy storage mechanism of supercapacitors is manifested as charge accumulation or reversible redox reactions, but the conventional double layer capacitive storage mechanism limits the practical application due to the low energy densities[6-8]. In order to further improve the energy

storage performance, great efforts have been made to investigate battery-like materials with high electrical conductivity and electroactivity with Faraday charge storage.

Among the nanomaterials for energy storage via Faraday reactions, transition metal phosphide (TMP) materials with high theoretical capacity and metal-like properties have been studied as viable supercapacitor battery-type materials[9]. Various types of monometallic phosphides (e.g., CoP, Cu_3P, etc.) with unique morphology and bimetallic phosphides (e.g., CoNiP) / trimetallic phosphides (e.g., CoNiZnP) with even higher electrical activity in ionic bond synergy have been extensively studied in the field of energy storage[10-13]. However, the diffusion behavior of these materials limits the electron transfer capability, leading to the undesired conductivity and cycle life[14, 15]. To address the issues, the introduction of highly electrically conductive or electrochemically active elements into battery materials shows considerable advantages in terms of accelerated reaction kinetics and improved electrical conductivity. In general, ion doping is capable of triggering changes in the electronic structure of metal phosphides and improving the adsorption free energy of intermediates, thus enhancing the activity and conductivity of TMPs[16, 17]. For example, Yan *et al.* designed Cu-doped CoP with nanosheet arrays, and found that the doping of Cu optimized the electronic structure and effectively improved the electrical conductivity, resulting in significant HER and OER catalytic activities[18]. Elshahawy *et al.* developed S-doped CoP nanotubes as high-performance energy storage materials, which exhibits high capacity and long stability[19]. Specifically, the doping of highly electronegative and active elements can optimize the charge density distribution, thus effectijvely

enhancing the capacitive contribution of phosphorus-based materials. On the other side, heterogeneous interface engineering is considered as a promising approach to reduce the activation energy and ion diffusion potential and accelerate the kinetic process of interfacial reactions[20, 21]. It is found that the introduction of phases with different energy levels could change the electronic structure to some extent and induce an embedded electric field at the interface, thus minimizing ion diffusion barriers and allowing heterogeneous composites with rich boundaries for optimization. For example, Gayathri et al. synthesized ZIF-derived leaf-like CoP_x/CoO heterostructures via a two-step low-temperature phase transformation, in which the successful construction of the heterostructures significantly changed the interfacial characteristics, thus improving the capacitance and durability during cycling[22]. Liu et $al.$ successfully synthesized in situ vertically grown Cu_3P/Ni_2P bimetallic phosphide nanosheets, revealing the capability of charge rearrangement at heterogeneous interfaces and the synergistic effect of hierarchical array structures on 3D substrates to promote overall hydrolysis[23]. Thus, constructing heterogeneous interfaces with intrinsically well-matched lattices is a promising mean to provide more favorable redox reactions with superior energy storage capacity.

Herein, we study the development of hollow core-shell $S-Co_2P@Ni_2P$ heterojunction with the introduction of S and Ni via ion exchange: (1) The hollow core-shell structure buffers bulk stress and increases the number of electroactive sites, providing a shortcut for electron transport and potentially enhancing the rate capability. (2) S doping into $Co_2P@Ni_2P$ promotes the interfacial charge transfer from the inner core of Co_2P to the

Ni_2P outer shell, in which the rearrangement of interfacial electrons optimizes the redox activity capacity of the active species, further accelerating the reaction kinetics. Consequently, the S-Co_2P@Ni_2P bimetallic phosphides exhibits promising electrochemical properties such as the specific capacitance of 1200 C g^{-1} at 1 A g^{-1}. In addition, the hybrid supercapacitor (HSC) fabricated using S-Co_2P@Ni_2P combined with activated carbon (AC) is developed to offer an excellent energy density of up to 41.5 Wh Kg^{-1} and retain 93% of the initial capacity after 15,000 cycles.

2. Results and discussion

2.1. Synthesis and characterization

The heterogeneous S-Co_2P@Ni_2P nanomaterials with the hollow core-shell structure synthesized by a combination of hydrothermal, ion exchange and low-temperature annealing methods are depicted in **Fig. 1**. All experimental details are presented in supporting information. Firstly, the arrays of cobalt hydroxide carbonate (CCHH) precursors with the nanoneedle-like structure are prepared by reacting $CoCl_2 \cdot 6H_2O$ with $CO(NH_2)_2$ at 120 °C for 6 h using a hydrothermal process. Secondly, an anion exchange reaction occurs between the precursor material and sodium sulfide by immersing the CCHH arrays into 0.1 M $Na_2S \cdot 9H_2O$ solution for 15 mins, and the inward diffusion of S^{2-} reconstructs the micromorphology, prompting the transformation of nanoneedles into nanoneedle spheres. The core-shell nanorods of S-CCHH@$Ni(OH)_2$ are obtained by chemical deposition of $Ni(OH)_2$ on the surface of the S-CCHH by heating in a water bath at 80 °C for 1 h. Finally, the PH_3 produced by the

decomposition of sodium hypophosphite during the annealing process is adsorbed on

the surface of the material and grow to obtain S-Co$_2$P@Ni$_2$P hollow shell

heterogeneous nanomaterials. The unique morphology and structure not only accelerate

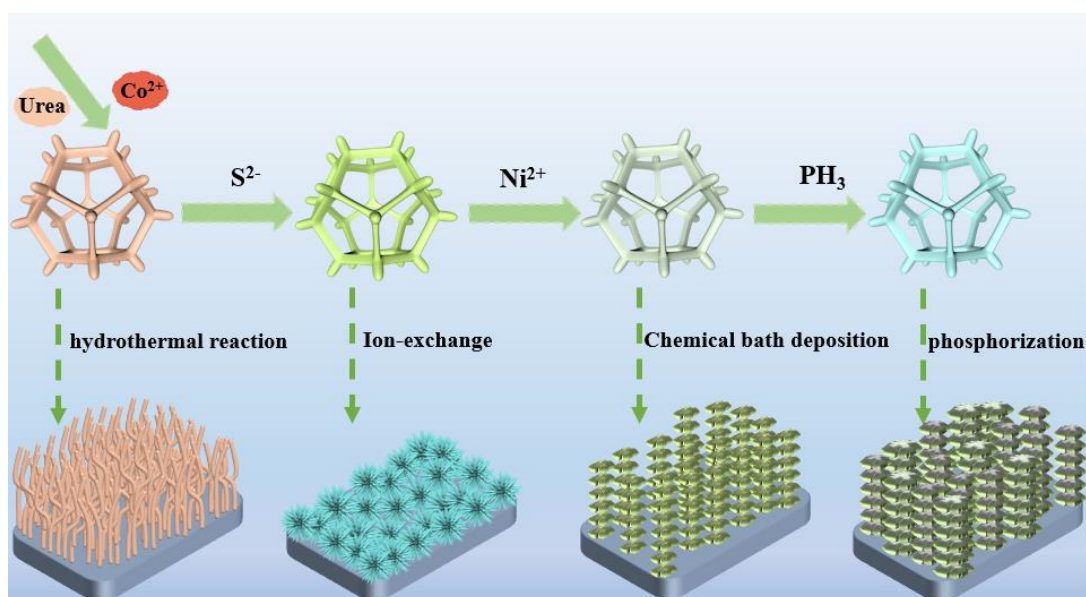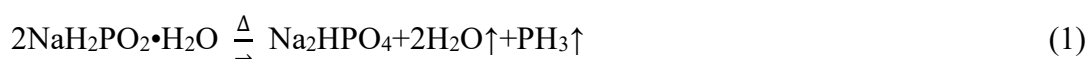the electrolyte transport, but also exhibit the stress-relieving effect of volume expansion.

$$2NaH_2PO_2 \cdot H_2O \xrightarrow{\Delta} Na_2HPO_4 + 2H_2O\uparrow + PH_3\uparrow \qquad (1)$$

$$M^{2+} + PH_3 \xrightarrow{\Delta} M_xP_y \ (M^{2+}=Ni^{2+}, Co^{2+}) \qquad (2)$$

Fig. 1. Schematic illustration of preparation of hollow core-shell S-Co$_2$P@Ni$_2$P heterojunction.

The crystal structures of the synthesized S-Co$_2$P@Ni$_2$P as well as the precursor as

shown in **Fig. 2a** are verified by X-ray diffraction (XRD). The CCHH precursor is in

good agreement with the corresponding standard card (JCPDS 48-0083). Similar XRD

patterns after doping confirm that the crystal structure is not affected by S doping, and

the characteristic peaks of Ni(OH)$_2$ after chemical deposition can be indexed by the

standard card (JCPDS 22-0444)[24]. Apparently, the main diffraction peaks of S-

Co$_2$P@Ni$_2$P can be attributed to Co$_2$P (JCPDS 54-0413) and Ni$_2$P (JCPDS 03-0953)

without obvious spurious peaks [25, 26]. **Fig. S1** shows the Rietveld refinement of the

S-Co$_2$P @Ni$_2$P. The refinement factors of χ^2, R$_{wp}$ and R$_p$ are 3.875, 4.35% and 3.28%, respectively, indicating that the calculated result match well with the experimental result. The contents ratio of the three phases of Ni, Ni$_2$P and Co$_2$P in the S-Co$_2$P @Ni$_2$P is 42:13:45. SEM images (**Fig. 2(b-c)**) show that the CCHH nanowires arrays are grown uniformly and interlaced on the NF, forming a one-dimensional hierarchical structure. The morphologies in **Fig. 2d and Fig. S2(a-b)** confirm that the doping of S leads to the transformation of the microstructure of the materials from nanowire to nanoflower. The abundant space between the three-dimensional structures facilitates the interface reaction of electrolyte, which makes it possible to achieve high-rate properties[27]. When the chemical deposition is performed, the nanosheets grow on the surface of nanorods such that the S-CCHH@Ni(OH)$_2$ morphology is further reconstructed into a nanocore-shell structure with a rougher surface compared to the CCHH nanorods (**Fig. 2e and Fig. S2(c-d)**). Finally, as shown in **Fig. 2(f-h),** after the phosphorylation, the S-Co$_2$P@Ni$_2$P inherits the core-shell nanorod morphology of the S-CCHH@Ni(OH)$_2$ with a diameter of 200 nm-300 nm and a rougher surface [28]. The three-dimensional core-shell nanostructure would enhance stability and electrochemical activity via accommodating the stress arising from the huge micromorphological changes and volume expansion during long-term cycling.
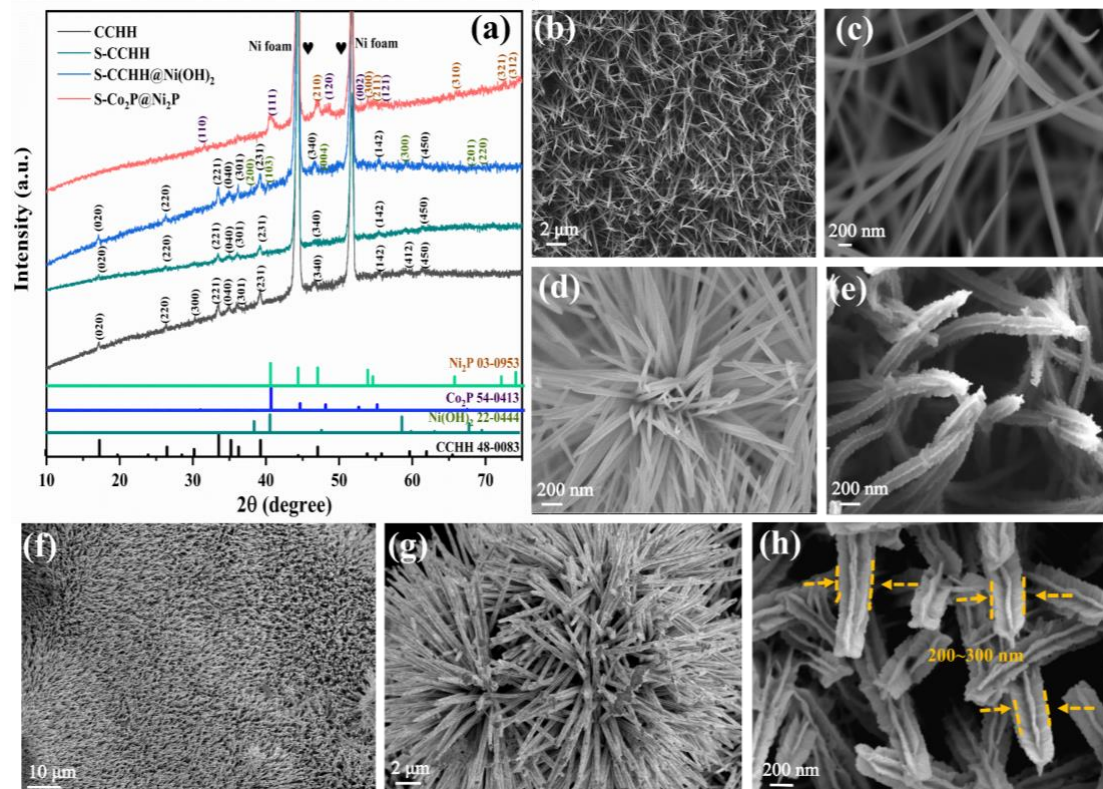
Fig. 2. (a) XRD patterns of the as-prepared S-Co$_2$P@Ni$_2$P and the precursors; SEM images of (b, c) CCHH; (d) S-CCHH; (e) S-CCHH@Ni(OH)$_2$ and (f, g, h) S-Co$_2$P@Ni$_2$P.

The TEM images could provide more detailed morphological interpretation of the S-Co$_2$P@Ni$_2$P nanomaterials. In **Fig. 3a**, S-Co$_2$P@Ni$_2$P shows the core-shell nanomorphology of hollow nanorods wrapped by nanosheets. **Fig. 3(b-c)** clearly show that a large number of irregular nanosheets adhering to the outer layer of the hollow nanorods, forming a well-defined core-shell interface. The diameters of the inner hollow nanorods and the whole core-shell structure are 70 nm and 200-300 nm, respectively, which are consistent with the SEM results. This conformation of the S-Co$_2$P@Ni$_2$P potentially enhances the rate capability by providing shortcuts for electron transport while buffering bulk stress. As displayed in **Fig. 3(d-e)**, the lattice stripes at 0.22 nm and 0.28 nm that are attributed to the (111) plane of Ni$_2$P and (110) crystal planes of Co$_2$P, respectively. A well-defined phase interface between Ni$_2$P and Co$_2$P can

be observed in the S-Co$_2$P@Ni$_2$P, revealing the successful establishment of a heterogeneous interface for the enhancement of ion diffusion. The obvious polycrystalline diffraction rings in the SAED pattern are also displayed in the Co$_2$P (111), Co$_2$P (120), Ni$_2$P (201), and Ni$_2$P (300) crystallographic planes, further verifying the formation of heterogeneous interfaces (**Fig. 3f**). In addition, the EDS and mapping images (**Fig. 3g and Fig. S3**) reflect the distribution of the elements Co, Ni, P, O, and S with homogeneity in S-Co$_2$P@Ni$_2$P. It can be seen that Co and S are concentrated in the core part of the S-Co$_2$P@Ni$_2$P hollow core-shell nanorods, while O, P and Ni elements are uniformly present throughout the heterogeneous core-shell structure, which is consistent with the experimental design idea. These results confirm that the hollow S-Co$_2$P@Ni$_2$P core-shell heterojunctions could be constructed successfully by ion exchange and phosphorylation. To further understand the microstructural characteristics of the S-Co$_2$P@Ni$_2$P material, the specific surface area and pore size distribution are investigated by Brunauer-Emmett-Teller (BET) measurements. As shown in **Fig. S4**, the S-Co$_2$P@Ni$_2$P hollow core-shell-structured material shows a typical type IV adsorption-desorption isotherm with a specific surface area of 5.10 m^2 g^{-1}. The pore size distribution of Barrett-Joyner-Halenda (BJH) calculated using the desorption curve indicates a mesoporous structure with a pore size of 8.45 nm [29]. These microstructural properties of the S-Co$_2$P@Ni$_2$P hollow core-shell material facilitate easy access of electrons and ions to the electrode/electrolyte interface.
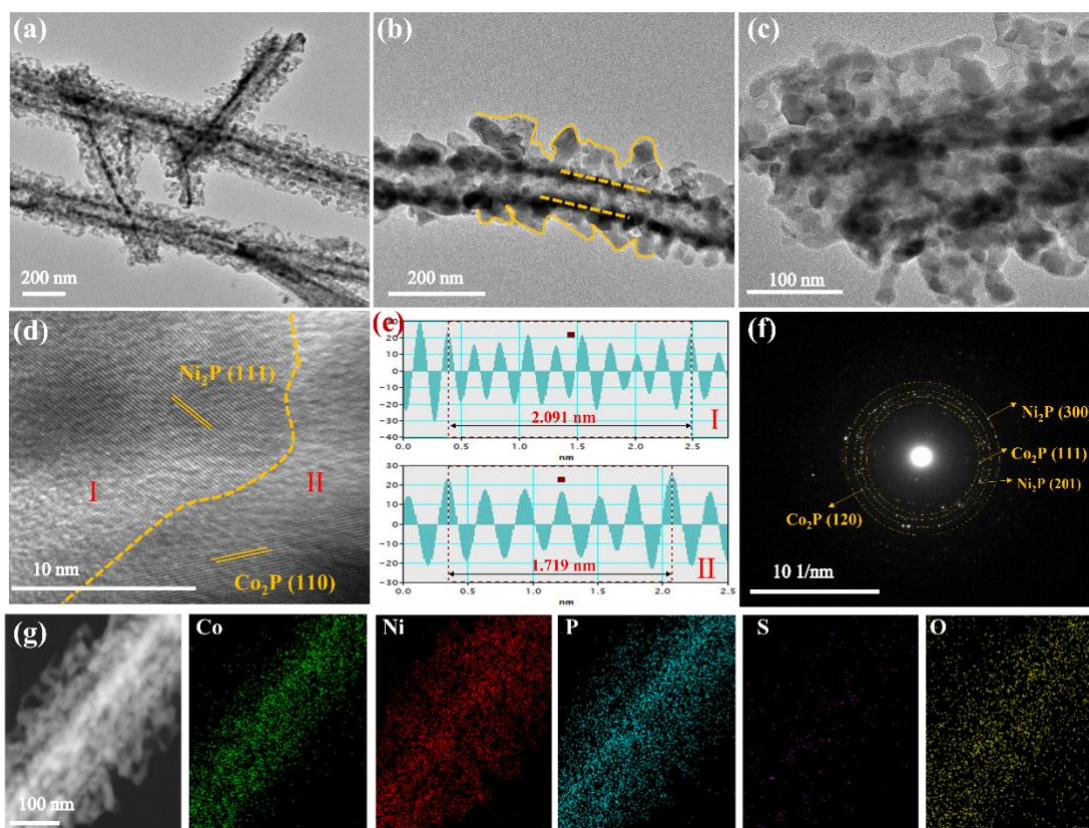
Fig. 3. (a, b, c) TEM images of S-Co$_2$P@Ni$_2$P hollow core-shell nanorods; (d, e) HRTEM image and corresponding fast Fourier transform (FFT) patterns of the S-Co$_2$P@Ni$_2$P hollow core-shell nanorod interface; (f) SAED pattern of S-Co$_2$P@Ni$_2$P; (g) Element mapping of S-Co$_2$P@Ni$_2$P.

The chemical composition and valence of the S-Co$_2$P@Ni$_2$P heterostructures are analyzed by XPS. As shown in **Fig. 4a**, Ni, Co, P, O and trace S elements exist in the sample in which the oxygen comes from phosphide that is easily oxidized in air and the small amount of S is due to the short ion exchange time, which are consistent with the results in **Fig. S3** and **Fig. 3f** [30]. As shown in **Fig. S5**, the spin-orbit peak of the spectrum of S 2p is located at 163.6 eV, while the peak at 171.6 eV belongs to the satellite peak of S^{2-} [31]. The fitted peaks of the S 2p orbital are relatively weak due to the low content of sulfur elements. The Co2p spectrum in **Fig. 4b** well explains the electronic characteristics in the presence of Co^{2+}/Co^{3+}. Compared with Co$_2$P@Ni$_2$P, the

two fitted peaks of Co $2p_{3/2}$ for S-Co$_2$P@Ni$_2$P are Co^{3+} (781.9 eV) and Co^{2+} (784.2 eV), respectively, and the two fitted peaks of Co $2p_{1/2}$ are Co^{3+} (797.1 eV) and Co^{2+} (800.1 eV), respectively. After incorporated with S, the peak area of Co^{3+} enlarges and the signal peak of Co 2p migrates to the high binding energy. The results show that the charge migrates from Co^{2+} to Co^{3+}, and the conversion equilibrium is induced by the doping [32]. Similarly, the Ni 2p map in **Fig. 4c** shows that the binding energies of 854.3 eV and 857.8 eV are well matched to Ni^{3+} and Ni^{2+} in S-Co$_2$P@Ni$_2$P belonging to the Ni $2p_{3/2}$, respectively, while the binding energies of 872.4 eV and 876.5 eV are assigned to Ni $2p_{1/2}$. Compared with Co$_2$P@Ni$_2$P, the peak shows an obvious transition to the lower binding energy, suggesting a strong electronic interaction between Co$_2$P and Ni$_2$P after S doping for charge redistribution to favor the electronic behavior of the modified material[33]. The P 2p patterns in **Fig. 4d** show that the P 2p peaks (129.9 eV and 131.4 eV) in the S-Co$_2$P@Ni$_2$P shift to higher binding energies compared to those in the Co$_2$P@Ni$_2$P such that electrons tend to move from Co$_2$P to Ni$_2$P (outer layer of material) to create a built-in electric field between the heterogeneous interfaces, resulting in more pronounced interfacial electron delocalization. This facilitates the acceleration of ion migration and optimizes the electrochemical process [34, 35]. The above results confirm the successful construction of the heterojunction between Co$_2$P and Ni$_2$P by the doping of S, and also emphasize the importance of electron structure redistribution to accelerate electron transfer and promote the synergistic effect of ions.
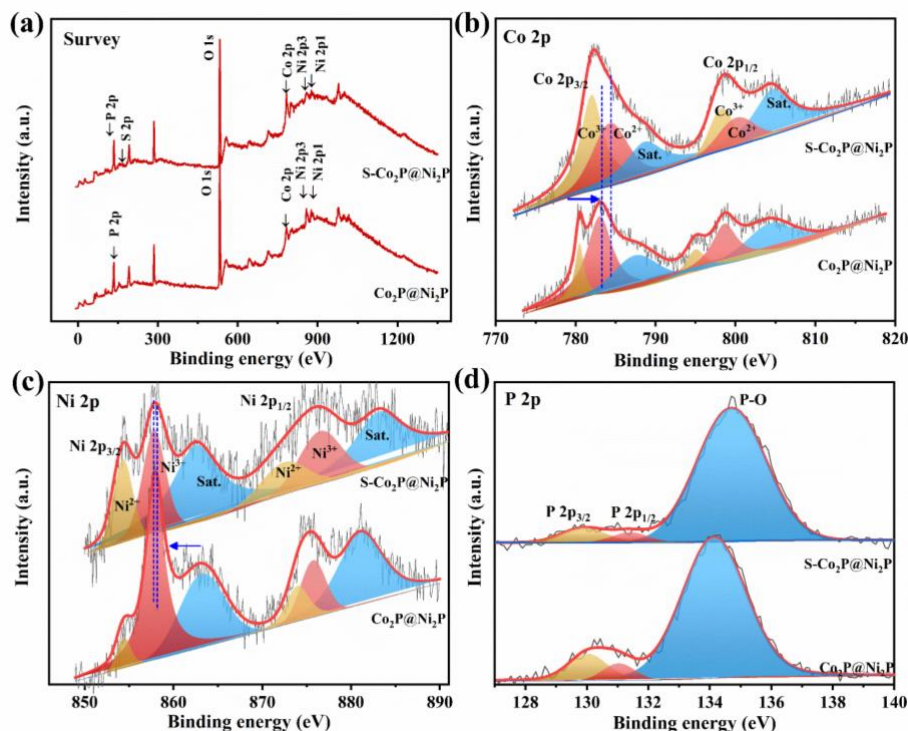
Fig. 4. XPS spectra of $Co_2P@Ni_2P$ and $S-Co_2P@Ni_2P$: (a) survey spectrum; (b) Co 2p; (c) Ni 2p and (d) P 2p.

2.2. Electrochemical performance testing

The electrochemical activity of the $S-Co_2P@Ni_2P$ hollow core-shell heterojunction is evaluated in a conventional three-electrode system. The electrochemical properties of the CCHH, S-CCHH, S-CCHH@Ni(OH)$_2$ and $S-Co_2P@Ni_2P$ nanomaterials at 5 mV s^{-1} are measured by cyclic voltammetry (CV) and shown in **Fig. 5a** and **Fig. S6 (a-c).** The redox peak of the $S-Co_2P@Ni_2P$ has a very pronounced potential difference compared to other samples, which may be due to the accelerated electron migration by the heterojunction effect. Besides, the $S-Co_2P@Ni_2P$ has the largest CV areal capacitance, which is associated with the fast charge storage promoted by S doping and the presence of weak M-P bonds in nickel-cobalt phosphide for easy conversion reactions[36, 37]. **Fig. 5b and Fig. S6 (d-f)** show the galvanostatic charge/discharge

(GCD) curves of various materials measured at a voltage plateau of 0.5 V for further analysis of energy storage capacity. The S-$Co_2P@Ni_2P$ has the longest discharge time due to the heterogeneous structure of hollow phosphide. Besides, the CV curves of the S-$Co_2P@Ni_2P$ for the increase of the sweep rate from 1 mV s^{-1}-10 mV s^{-1} exhibit distinct redox peaks, inferring that the electrode material has the battery-like behavior **(Fig. 5c)**. Moreover, the similarity of the CV curves confers excellent response reversibility and high-rate peculiarity. The GCD curves of S-$Co_2P@Ni_2P$ at current densities of 1-10 A g^{-1} are shown in **Fig. 5d**, accompanied by a distinct discharge plateau, demonstrating the typical battery-type behavior characteristics. For a fair comparison, the electrochemical properties of S-Co_2P and $Co_2P@Ni_2P$ are tested, displayed in **Fig. S7**, confirming the positive effects of introducing S in the S-$Co_2P@Ni_2P$ nanomaterials for enhance conductivity and reaction reversibility. The S-$Co_2P@Ni_2P$ hollow core-shell heterojunction exhibits the most excellent specific capacity of 1200 C g^{-1} at 1 A g^{-1}, which is superior to CCHH nanorods (613 C g^{-1}), S-CCHH nanoflowers (729 C g^{-1}), and S-CCHH@$Ni(OH)_2$ core-shell structure (1127 C g^{-1}) electrodes. The specific capacity of S-$Co_2P@Ni_2P$ can still reach 910 C g^{-1} when the current density is 10 A g^{-1}. Compared with the CCHH (37.5%), S-CCHH (62%) and S-CCHH@$Ni(OH)_2$ (54%), the S-$Co_2P@Ni_2P$ possesses the capacity retention of 76%, indicating that the S doping and synergistic effect with the highly electrochemically active nickel-cobalt phosphide accelerates charge transfer and improves electrical conductivity(**Fig. 5(e-f)**)[38]. Based on the plots ($i = av^b$) of peak current (i) and scanning speed (v), the values of b of all four materials are positive with the range of 0.5-1[39, 40]. The value of b of the S-

13

Co$_2$P@Ni$_2$P is 0.68, indicating that the nanomaterials act via both the diffusion control and pseudocapacitance mechanisms such that the reversible intercalation and release of ions and Faradaic redox reactions ensure the high capacity of the S-Co$_2$P@Ni$_2$P hollow core-shell heterojunction (**Fig. 5g**). The contributions of diffusion control and capacitance to the total charge storage are quantified according to the equation $I(V) = k_1 v + k_2 v^{1/2}$[41], where $I(V)$, v and k refers to the response current, scanning rate and controllable constants, respectively. **Fig. 5h** shows that the pseudocapacitance contribution of the S-Co$_2$P@Ni$_2$P heterogeneous material is able to reach 52% at 3 mV s^{-1}. As the scan rate increases, the ratio of pseudocapacitance increases from 40% to 83%, confirming that the S-Co$_2$P@Ni$_2$P electrode has fast reaction kinetics (**Fig. 5i and Fig. S8**). In the case of S doping, the effective binding of Co and Ni metal atoms with different d-band distributions may lead to different degrees of charge transfer, and the construction of multi-heterogeneous interfaces excites built-in field effects, ultimately optimizing the diffusion of OH$^-$ and the ability of reversible redox activities[42].
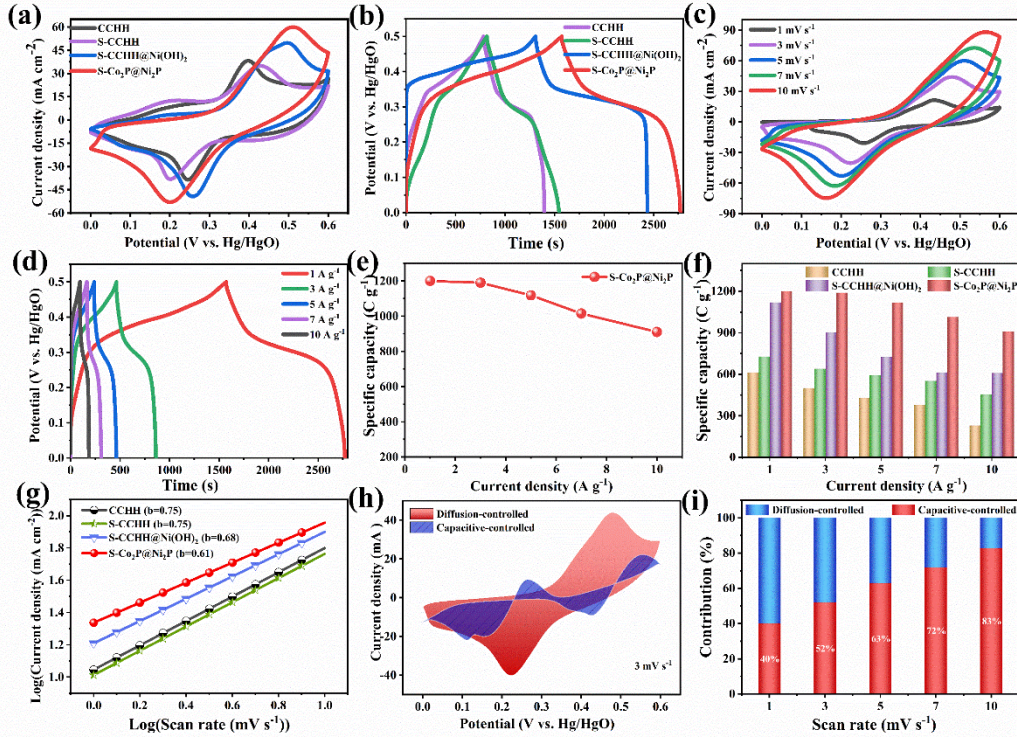
Fig. 5. (a) CV curves of CCHH, S-CCHH, S-CCHH@Ni(OH)$_2$ and S-Co$_2$P@Ni$_2$P electrodes (5 mV s^{-1}) ; (b) GCD curves of CCHH, S-CCHH, S-CCHH@Ni(OH)$_2$ and S-Co$_2$P@Ni$_2$P electrodes (1 A g^{-1}); (c) CV curves of S-Co$_2$P@Ni$_2$P electrodes from 1 to 10 mV s^{-1}; (d) GCD curves of S-Co$_2$P@Ni$_2$P electrodes from 1 to 10 A g^{-1}; (e, f) Specific capacity CCHH, S-CCHH, S-CCHH@Ni(OH)$_2$ and S-Co$_2$P@Ni$_2$P electrodes as a function of current density; (g) Power-law relationship between peak current and sweep rate for CCHH, S-CCHH, S-CCHH@Ni(OH)$_2$, and S-Co$_2$P@Ni$_2$P electrodes; (h) Capacitance contribution of S-Co$_2$P@Ni$_2$P at 3 mV s^{-1} as a percentage of total charge storage; (i) Relative contribution of charge storage process of S-Co$_2$P@Ni$_2$P electrodes at different sweep rates.

Fig. 6a shows the impedance results fitted using Nyquist plots and EIS circuit models to analyze the kinetic properties of the S-Co$_2$P@Ni$_2$P[43, 44]. The results indicate that the four electrodes show similar Rs values, whereas the Rct of S-Co$_2$P@Ni$_2$P nanomaterial (0.225 Ω) is the smallest among S-CCHH (0.500 Ω), S-CCHH@Ni(OH)$_2$ (0.912 Ω), and CCHH (1.202 Ω). Obviously, the hollow heterogeneous configuration effectively enhances the diffusion and transport kinetics of electrolyte ions. The S-

15

$Co_2P@Ni_2P$ heterojunction with the core-shell hollow structure favors carrier migration due to the unique microstructure and sulfur doping, resulting in good electrical conductivity and electrochemical properties (**Fig. 6b**). To show the significance of our proposed work, the long-cycle performance of the $S-Co_2P@Ni_2P$ heterojunction material is explored. As shown in **Fig. 6c**, the capacity retention of the $S-Co_2P@Ni_2P$ reaches 80.5% after 4700 cycles. Compared with CoP/Mo-NiCoP nanoplate arrays (892.6 C g^{-1}), NiCoP hollow cubes (629 C g^{-1}), NiCoP/NPC hollow spheres (660.3 C g^{-1}), $V-Ni_{12}P_5$ nanosheets (727.5 C g^{-1}), Ni_2P/Ni/C hollow spheres (724. 5 C g^{-1}), P-$MnCo_2O_4$ nanotubes (498.4 C g^{-1}), $Zn_xCo_{3-x}S_4$ hollow dodecahedra (545.9 C g^{-1}) and O-NiCoP@rGO particles (831.6 C g^{-1}), the $S-Co_2P@Ni_2P$ with much higher specific capacity (**Fig. 6d** and **Table S1**)[37, 45-52]. The origins of significant positive effects on the performance can be interpreted as follows: (1) the $S-Co_2P@Ni_2P$ with the three-dimensional NF substrate is binder-free to avoid the dead volume and retain the stability; (2) the hollow core-shell structure allows an increase in the effective contact area, promoting the wetting effect of the electrolyte and shortening the transport path; and (3) the induced redistribution of the electronic structure has a positive effect on improving the capacitive behavior and reaction kinetics. The combination of hollow core-shell microstructure and heterogeneous phases can provide more charge compensation, leading to more charge storage. These results demonstrate that the $S-Co_2P@Ni_2P$ heterojunction material is beneficial for the construction of high-performance hybrid supercapacitors.
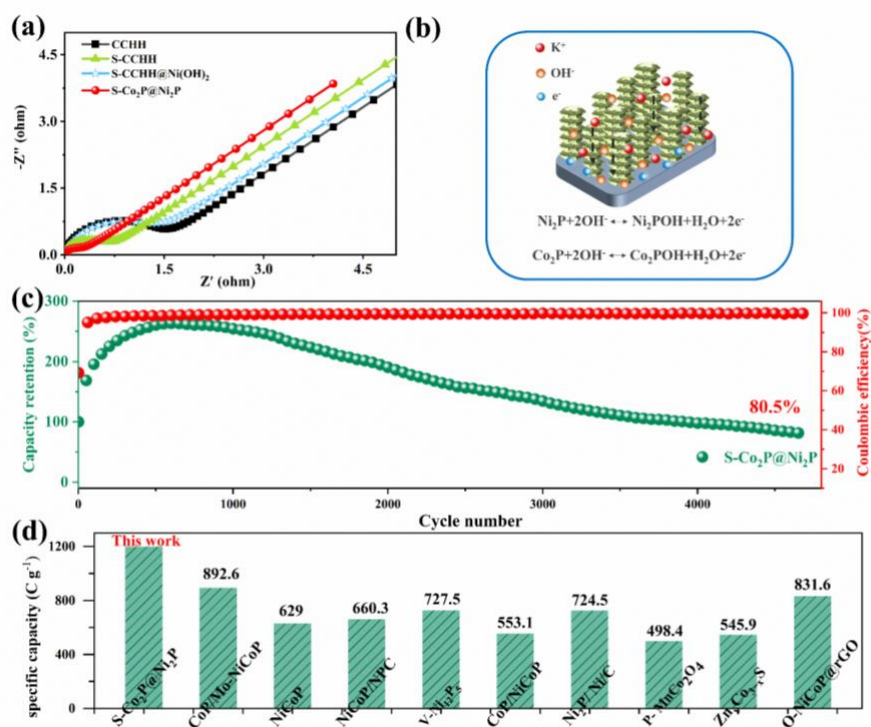
16

Fig. 6. (a) EIS spectra of CCHH, S-CCHH, S-CCHH@Ni(OH)$_2$ and S-Co$_2$P@Ni$_2$P electrodes; (b) Schematic diagram of the electron diffusion mechanism of S-Co$_2$P@Ni$_2$P hollow core-shell heterojunction electrode; (c) Cycling stability of S-Co$_2$P@Ni$_2$P electrode (9 A g^{-1}); (d) Capacity values of S-Co$_2$P@Ni$_2$P electrodes compared with those of similar electrodes reported previously.

2.3. Electrochemical performance of S-Co$_2$P@Ni$_2$P //AC device

The AC/NF anode material is firstly prepared and tested for electrochemical properties with a capacitance value of 350 F g^{-1} at 1 A g^{-1}. The CV and GCD curves shown in **Fig. S9(a-b)** illustrate the bilayer properties of the material. Immediately after, an electrochemical-driven hybrid S-Co$_2$P@Ni$_2$P //AC supercapacitor as shown in **Fig. 7a** is assembled to verify its potential. By exploiting the synergies between the double-layer electric and battery-type electrodes, the actual operating voltage range of the device is substantially expanded (**Fig. S9c**). As expected, **Fig. 7b** shows that no polarization is observed in the voltage range 0-1.6 V for the CV plot of the device

17

obtained at 10 mV s^{-1}. Besides, the GCD curves for voltage windows from 0-1.2 to 0-1.6 V collected at a current density of 1 A g^{-1} confirm a maximum operating voltage of up to 1.6 V (**Fig. 7c**). **Fig. 7d** is presented as the CV curves of the device at the scan rate of 5-50 mV s^{-1}, in which the redox peak and rectangular shape are retained in the voltage interval of 0-1.6 V, demonstrating the advantages of the Faraday mechanism and the electrochemical double layer capacitive behavior. As shown in **Fig. 7e**, the GCD curves tested a current density of 1-10 A g^{-1} are almost symmetric, demonstrating the satisfactory high reversibility and Coulomb efficiency of the assembled devices. The device possesses an excellent specific capacitance of 117 F g^{-1} at 1 A g^{-1} as calculated from the discharge curve (**Fig. S9d**). Impressively, the device also displays an energy density of 41.5 Wh kg^{-1} at a power density of 797.8 W kg^{-1} and reaches a power density of 8043.4 W kg^{-1} at an energy density of 15.6 Wh kg^{-1}. The energy and power densities of the S-Co$_2$P@Ni$_2$P//AC device are compared with the literatures as shown in the Ragone plot (**Fig. 7f**) and **Table S2**, showing the great advantages of the TMP-based materials[15, 22, 53-55]. In addition, as the cycling stability is critical in the evaluation of the durability of commercial HSC devices, the S-Co$_2$P@Ni$_2$P//AC device is tested in continuous charge/discharge cycles at 2 A g^{-1}. As depicted in **Fig. 7g**, the device exhibits a capacity retention rate of 93% and a coulombic efficiency of nearly 100% after 15,000 cycles, confirming its remarkable stability. The S-Co$_2$P@Ni$_2$P cycled for 15,000 cycles is further characterized by XPS (**Fig. S10 and S11**). It can be seen that after cycling, the signals of phosphide peak in the P 2p regions become weak, while those of Co^{3+} and Ni^{2+} are stronger, which may be attributed to the oxidation of the

18

material due to the contact reaction between the electrode and the electrolyte[56]. In addition, the essentially constant active components and similar peak states of the materials before and after cycling indicate good structural stability. As expected, the microscopic morphology of the S-Co$_2$P@Ni$_2$P after cycling is similar to that of the material before cycling, showing excellent microstructural stability ((**Fig. S12**)). To further demonstrate the potential of applicability, the HSC device successfully lit the red and blue light-emitting diodes (LEDs) in succession (insets of **Fig. 7g**).
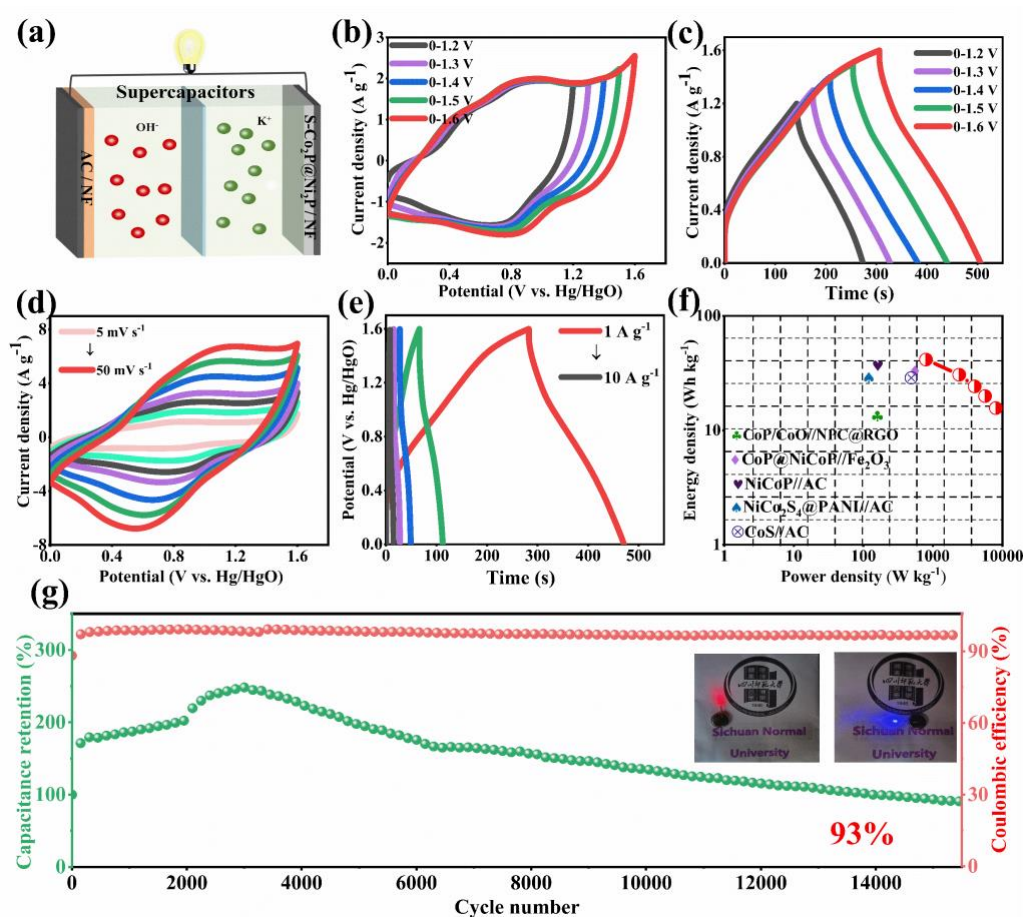
Fig. 7. (a) Display diagram of S-Co$_2$P@Ni$_2$P//AC device; (b) CV curves of the device at different voltages measured at 10 mV s^{-1}; (c) GCD curves of the device at different voltages measured at 1 A g^{-1}; (d) CV curves of the device at different scan rates; (e) GCD curves of the device at different current densities; (f) Comparison of energy density and power density of the devices with the reported ones; (g) Long-cycle performance of the device up to 15,000 cycles (insets show the device

19

lit the LEDs).

3. Conclusion

In conclusion, we have successfully synthesized S-Co$_2$P@Ni$_2$P hollow core-shell heterogeneous battery-type materials via hydrothermal, ion exchange and annealing treatments. The hollow core-shell microstructure relieves the stress caused by volume change during electrochemical reactions and promotes the infiltration of electrolyte into the electrode to enhance the structural stability of the material. Moreover, the introduction of sulfur promotes the charge transfer from the Co$_2$P core to the Ni$_2$P outer layer, improving the conductivity and reaction kinetics by regulating the electronic structure of the interface; and the construction of phosphide further enhances the electrical conductivity. Thanks to the above unique structure and composition advantages induced by non-metallic S and phosphorylation, the S-Co$_2$P@Ni$_2$P exhibits an excellent specific capacity of 1200 C g^{-1} at 1 A g^{-1}. The HSC device of the S-Co$_2$P@Ni$_2$P//AC exhibits an energy density of up to 41.5 Wh kg^{-1} at a power density of 797.8 W kg^{-1}, demonstrating excellent stability of electrochemical performance (the capacity is maintained at 93% of the initial after 15,000 cycles). This work not only provides a useful reference for modulating the electronic structure of battery-type electrode materials, but also presents valuable insights into the exquisite design of bimetallic phosphide heterojunctions with high performance.

Conflicts of interest

There are no conflicts to declare.

References

[1] Y. Shao, M.F. El-Kady, J. Sun, Y. Li, Q. Zhang, M. Zhu, H. Wang, B. Dunn, R.B. Kaner, Design and Mechanisms of Asymmetric Supercapacitors, Chem. Rev. 118 (2018) 9233-9280.

[2] N. Choudhary, C. Li, J. Moore, N. Nagaiah, L. Zhai, Y. Jung, J. Thomas, Asymmetric Supercapacitor Electrodes and Devices, Adv. Mater. 29 (2017) 1605336.

[3] Y. Wang, Y. Song, Y. Xia, Electrochemical capacitors: mechanism, materials, systems, characterization and applications, Chem. Soc Rev. 45 (2016) 5925-5950.

[4] H. Liu, S. Wang, H. Liu, L. Li, Transition metal based battery-type electrodes in hybrid supercapacitors: A review, Energy Storage Mater. 28 (2020) 122-145.

[5] M. Zhong, Miao. Zhang, X. Li, Carbon nanomaterials and their composites for supercapacitors, Carbon Energy (2022) 1-36.

[6] D.P. Chatterjee, A.K. Nandi, A review on the recent advances in hybrid supercapacitors, J. Mater. Chem. A 9 (2021) 15880.

[7] M. Salanne, K. Naoi, K. Kaneko, P.-L. Taberna, C. P. Grey, B. Dunn and P. Simon, Efficient storage mechanisms for building better supercapacitors, Nat. energy 1 (2016) 16070.

[8] T. Nguyen, M.F. Montemor, Metal Oxide and Hydroxide-Based Aqueous Supercapacitors: From Charge Storage Mechanisms and Functional Electrode Engineering to Need-Tailored Devices, Adv. Sci. 6 (2019) 1801797.

[9] Q. Zong, C. Liu, H. Yang, Q. Zhang, G. Cao, Tailoring nanostructured transition metal phosphides for high-performance hybrid supercapacitors, Nano Today 38 (2021) 101201.

[10] R. Sahoo, D.T. Pham, T.H. Lee, T.H.T. Luu, J. Seok, Y.H. Lee, Redox-Driven Route for Widening Voltage Window in Asymmetric Supercapacitor, ACS Nano 12 (2018) 8494-8505.

[11] N. R. Chodankar , S. J. Patil , S. K. Hwang, G. S. R. Raju, K. S. Ranjith, D. P. Dubal, Y. S. Huh,Y. K. Han, Solution-free self-assembled growth of ordered tricopper phosphide for efficient and stable hybrid supercapacitor, Energy Storage Mater. 39 (2021) 194–202.

[12] Z. Wang, S. Ji , X. Wang, P. Zhou, S. Huo,V. Linkov, R. Wang, Hollow-structured NiCoP nanorods as high-performance electrodes for asymmetric supercapacitors, Mater. Design 193 (2020) 108807.

[13] B. Chen, Z. Zhang, M. Lee, K. Yong, MOF-derived NiCoZnP nanoclusters anchored on hierarchical N-doped carbon nanosheets array as bifunctional electrocatalysts for overall water splitting, Chem. Eng. J. 422 (2021) 130533.

[14] C. Wang, G. Sui, D. Guo, J. Li, L. Zhang, S. Li, J. Xin, D.F. Chai, W. Guo, Structure-designed synthesis of hollow/porous cobalt sulfide/phosphide based materials for optimizing supercapacitor storage properties and hydrogen evolution reaction, J. Colloid Interface Sci. 599 (2021) 577-585.

[15] P. Lia, H. Yin, J. Yao, X. Liu, S. Chen,, Hierarchical mesoporous NiCoP hollow nanocubes as efficient and stable electrodes for high-performance hybrid supercapacitor, Appl. Surf. Sci. 536 (2021) 147751.

[16] X. Xiao, L. Tao, M. Li, X. Lv, D. Huang, X. Jiang, H. Pan, M. Wang, Y. Shen, Electronic modulation of transition metal phosphide via doping as efficient and pH-universal electrocatalysts for hydrogen evolution reaction, Chem. Sci. 9 (2018) 1970-1975.

[17] A. L. Lyu, B. H. Lee, C. W. Kim, E. Jung, K. d. Seong, T. Hyeon, and Y. Piao, Zeolitic Imidazole Framework Sacrificial Template-Assisted Synthesis of NiCoP Nanocages Doped with Multiple Metals for High Performance Hybrid Supercapacitors, ACS Appl. Energy Mater. 4 (2021) 10553−10564.

[18] L. Yan, J. Zhu, Y. Li, P. Tsiakaras, P. Shen, Electronic modulation of cobalt phosphide nanosheet arrays via copper doping for highly efficient neutral-pH overall water splitting, Appl. Catal. B Environ. 265 (2020) 118555.

[19] A. M. Elshahawy, X. Li, H. Zhang, Y. Hu, H. Wu, S. J. Pennycook, J. Wang, Sulfur-

doped cobalt phosphide nanotube arrays for highly stable hybrid supercapacitor, Nano Energy 39 (2017) 162-171.

[20] X. Zhou, X. Yue, Y. Dong, Q. Zheng, D. Lin, X. Du, G. Qu, Enhancing electrochemical performance of electrode material via combining defect and heterojunction engineering for supercapacitors, J. Colloid Interface Sci. 599 (2021) 68-78.

[21] F. Xiang, Y. Dong, X. Yue, Q. Zheng, D. Lin, High-capacity CoP-Mn_3P nanoclusters heterostructures derived by Co_2MnO_4 as advanced electrodes for supercapacitors, J. Colloid Interface Sci. 611 (2022) 654-661.

[22] S. Gayathri, P. Arunkumar, D. Saha, J.H. Han, Composition engineering of ZIF-derived cobalt phosphide/cobalt monoxide heterostructures for high-performance asymmetric supercapacitors, J. Colloid Interface Sci. 588 (2021) 557-570.

[23] H. Liu, X. Xu, Q. Jia, L. Yang , S. Wang, D. Cao, Oriented construction Cu_3P and Ni_2P heterojunction to boost overall water splitting, Chem. Eng. J. 448 (2022) 137706.

[24] W.L. K. Song, J. Xin, Y. Zheng, X. Chen, R. Yang, W. Lv, Q. Li, Hierarchical porous heterostructured $Co(OH)_2$/$CoSe_2$ nanoarray: A controllable design electrode for advanced asymmetrical supercapacitors, Chem. Eng. J. 419 (2021) 129435.

[25] T. Wang, C. Wang, Y. Ni, Y. Zhou, B. Geng, Hexamethylenetetramine induced multidimensional defects in Co_2P nanosheets for efficient alkaline hydrogen evolution, Chem. Commun. 58 (2022) 6352-6355.

[26] Y. Jin, L. Wang, Q. Jiang, C. Ji, X. He, Preparation of mesoporous Ni_2P nanobelts with high performance for electrocatalytic hydrogen evolution and supercapacitor, int. j. hydrogen energy 43 (2018) 3697-3704.

[27] P. Sun, L.Wang, J. Zhang, J. Huang, P. Wang, J. Hou, J. Zhang, C. Li, Z. Yao, Y. Yang, J. Xiong, Metal-organic frameworks derived copper doped cobalt phosphide nanosheet arrays with boosted electrochemical performance for hybrid supercapacitors, Electrochim. Acta 363 (2020) 137262.

[28] A. D. Savariraj, R. Manikandan. C. J. Raj, R. Velayutham, R. V. Mangalaraja, J. Park, W-J. Cho, B. C. Kim, Epitaxial Engineering Strategy to Amplify Localized

Surface Plasmon Resonance and Electrocatalytic Activity Enhancement in Layered Bismuth Selenide by Phosphorus Functionalization, Batteries & Supercaps 5 (2022) 202100310.

[29] X. Liu, X. Lu, X. He, N. Jiang, Y. Huo, C. Xu, D. Lin, Metal-organic framework derived in-situ nitrogen-doped carbonencapsulated CuS nanoparticles as high-rate and long-life anode for sodium ion batteries, J. Alloys Compd. 854 (2021) 157132.

[30] C. Li, Y. Yan, P. Huo, X. Wang, MOF-derived NiZnCo-P nano-array for asymmetric supercapacitor, Chem. Eng. J. 446 (2022) 137108.

[31] G. Xiang, G. Qu, J. Yin, B. Teng, Q. Wei, X. Xu, Dual-functional $NiCo_2S_4$ polyhedral architecture with superior electrochemical performance for supercapacitors and lithium-ion batteries, Science Bulletin 65 (2020) 443–451.

[32] J. Zhao, Z. Zhang, Y. Liu, J. Song, T. Liu, Y. He, A. Meng, C. Sun, M. Hu, L. Wang, G. Li, J. Huang, and Z. Li, The Semicoherent Interface and Vacancy Engineering for Constructing $Ni(Co)Se_2@Co(Ni)Se_2$ Heterojunction as Ultrahigh-Rate Battery-Type Supercapacitor Cathode, Adv. Funct. Mater. (2022) 2202063.

[33] Z. Xu, H. Yang, J. Huang, X. Zhang, J. Chen, NiCoP@CoS tree-like core-shell nanoarrays on nickel foam as battery-type electrodes for supercapacitors, Chem. Eng. J. 421 (2021) 127871.

[34] Q. Li, Interfacial Control of NiCoP@NiCoP Core-Shell Nanoflake Arrays as Advanced Cathodes for Ultrahigh-Energy-Density Fiber-Shaped Asymmetric Supercapacitors, Small 17 (2021) e2101617.

[35] L. Wang, X. Liu, J. Gu, R. Si, Y. Qiu, Y. Qiu, D. Shi, F. Chen, X. Sun, J. Lin, J. Sun, Atomically Dispersed Mo Supported on Metallic Co_9S_8 Nanoflakes as an Advanced Noble-Metal-Free Bifunctional Water Splitting Catalyst Working in Universal pH Conditions, Adv. Energy Mater. 10 (2019) 1903137.

[36] R. Manikandan, C. J. Raj. A. D. Savariraj, P. Thondaiman, W-J. Cho, H-M. Jang, B. C. Kim, Template assisted synthesis of porous termite nest-like manganese cobalt phosphide as binder-free electrode for supercapacitors, Electrochim. Acta 393 (2021) 139060.

[37] S. Hou, M. Wang, Y. Xu, T. Lu, Y. Yao and L. Pan, Carbon-incorporated Janus-type Ni_2P/Ni hollow spheres for high performance hybrid supercapacitors, J. Mater. Chem. A 5 (2017) 19054.

[38] Y. Yang, S. Li, W. Huang, S. Duan, P. Si, L. Ci, Rational construction of ternary ZnNiP arrayed structures derived from 2D MOFs for advanced hybrid supercapacitors and Zn batteries, Electrochim. Acta 387 (2021) 138548.

[39] Y. Li, J. Chen, Q. Zheng, Y. Huo, F. Xie, D. Lin, Polyaniline intercalation induced great enhancement of electrochemical properties in ammonium vanadate nanosheets as an advanced cathode for high-performance aqueous zinc-ion batteries, Chem. Eng. J. 448 (2022) 137681.

[40] S. Ding, Y. Feng, X. Yue, Q. Zheng, Q. Hu, D. Lin, Electric-Field-Assisted Alkaline Hydrolysis of Metal-Organic Framework Bulk into Highly Porous Hydroxide for Energy Storage and Electrocatalysis, Inorg. Chem. 61 (2022) 4948-4956.

[41] X. Li, R. Deng, X. Wei, X. Liu, Q. Zheng, D. Lin, Y. Song, Metal organic frameworks-derived multi-shell copper-cobalt-zinc sulfide cubes for sodium-ion battery anode, Chem. Eng. J. 425 (2021) 131501.

[42] M. Zhao, J. Li, W. Hu, C.M. Li,, Strong Electronic Interaction Enhanced Electrocatalysis of Metal Sulfide Clusters Embedded Metal-Organic Framework Ultrathin Nanosheets toward Highly Efficient Overall Water Splitting, Adv. Sci. 7 (2020) 2001965.

[43] Y. Xiang, Q. Li, X. Wei, X. Li, Q. Zheng, Y. Huo, D. Lin, Constructing $NiS_2/NiSe_2$ heteroboxes with phase boundaries for Sodium-Ion batteries, J. Colloid Interface Sci. 607 (2022) 752-759.

[44] X. Liu, J. Gong, X. Wei, L. Ni, H. Chen, Q. Zheng, C. Xu, D. Lin, MoO_4^{2-}-mediated engineering of $Na_3V_2(PO_4)_3$ as advanced cathode materials for sodium-ion batteries, J. Colloid Interface Sci. 606 (2022) 1897-1905.

[45] Y. Zhao, J. Yua, R. Chen, Q. Liu, J. Liu, R. Li, X. Wang, J. Wang, Binder-free metal-organic frameworks-derived CoP/Mo-doped NiCoP nanoplates for high-performance quasi-solid-state supercapacitors, Electrochim. Acta 390 (2021) 138840.

[46] X. Zhang, L. Zhang, G. Xu, A. Zhao, S. Zhang, T. Zhao, Template synthesis of structure-controlled 3D hollow nickel-cobalt phosphides microcubes for high-performance supercapacitors, J. Colloid Interface Sci. 561 (2020) 23-31.

[47] M. Yi, X. Zhang, Y. Tan, Z. Zhua, Z. Pan, J. Zhang, Ionic liquid-assisted synthesis of nickel cobalt phosphide embedded in N, P codoped-carbon with hollow and folded structures for efficient hydrogen evolution reaction and supercapacitor, Appl. Catal. B Environ. 283 (2021) 119635.

[48] S.K. M. Afshan, SK T.Aziz, R. Ghosh, M. Pahuja, S. A. Siddiqui, K. Alam, S. Rani, D. Rani, T. Maruyama, Sk Riyajuddin, and K. Ghosh, Boosting the Supercapacitive Performance via Incorporation of Vanadium in Nickel Phosphide Nanoflakes: A High-Performance Flexible Renewable Energy Storage Device, Energy Fuels 36 (2022) 4076-4086.

[49] Y. Lin, S. Liu, X. Chen, Y. Cheng, W. C. Cheong, Z. Chen, L. Zheng, J. Zhang, X. Li, Y. Pan, and C. Chen, Construction of CoP/NiCoP Nanotadpoles Heterojunction Interface for Wide pH Hydrogen Evolution Electrocatalysis and Supercapacitor, Adv. Energy Mater. (2019) 1901213.

[50] W. Feng, Y. Zheng, H. W, L. Li, X. Wei, Excellent rate capability supercapacitor electrodes with highly hydroxyl ion adsorption capacity enabled by P-doped $MnCo_2O_4$ nanotube arrays, Appl. Surf. Sci. 599 (2022) 153908.

[51] X. Qian, Y. Lu, J. Xia, B. Huang, J. Sun, G. He, H. Chen, Construction of sulfur vacancies enriched hollow zinc cobalt bimetallic sulfides for high-performance supercapacitors, J. Alloys Compd. 913 (2022) 165191.

[52] Y. Zhang, L. Zhang, X. Li, J. Gu, H. Si, L. Wu, Y. Shi, C. Sun, Y. Zhang, Highly porous oxygen-doped NiCoP immobilized in reduced graphene oxide for supercapacitive energy storage, Compos. Part B: Eng. 182 (2020) 107611.

[53] X. Wang, W. Zhang, X. Wang, X. Liu, B. Dong, Y. Zhang, One-step phosphorization synthesis of CoP@NiCoP nanowire/nanosheet composites hybrid arrays on Ni foam for high-performance supercapacitors, Appl. Surf. Sci. 532 (2020) 147437.

[54] X. Huang, High performance asymmetric supercapacitor based on hierarchical flower-like $NiCo_2S_4$@polyaniline, Appl. Surf. Sci. 487 (2019) 68-76.

[55] Z. Jiang, Z. Li, K. Ho, X. Li, X. Jiao and D. Chen, Synthesis of amorphous cobalt sulfide polyhedral nanocages for high performance supercapacitors, J. Mater. Chem. A 2 (2014) 8603.

[56] F. Pan, H. He, Z. Yang, Q. Zheng, D. Lin, Y. Huo, Rationally designed $Ni_2P/WS_2/Co_9S_8$@C multi-interfacial electrocatalyst for efficient overall water splitting, Chem. Eng. j. 446 (2022) 136961.